Hindawi Publishing Corporation
Journal of Nanomaterials
Volume 2015, Article ID 617130, 10 pages
http://dx.doi.org/10.1155/2015/617130

Research Article

Nanomaterial Host Bands Effect on the Photoluminescence Properties of Ce-Doped YAG Nanophosphor Synthesized by Sol-Gel Method

L. Guerbous and A. Boukerika

Laser Department, Nuclear Research Centre of Algiers (CRNA), 02 Boulevard Frantz Fanon, BP 399, 16000 Algiers, Algeria

Correspondence should be addressed to L. Guerbous; guerbous@yahoo.fr

Received 10 November 2014; Revised 12 March 2015; Accepted 12 March 2015

Academic Editor: Chuanbao Cao

Cerium trivalent (Ce^{3+}) doped YAG nano-sized phosphors have been successfully synthesized by sol-gel method using different annealing temperatures. The samples have been characterized by X-ray diffraction (XRD), thermogravimetry (TG), differential scanning calorimetry (DSC) analysis, Fourier transform infrared (FTIR) spectroscopy, and steady photoluminescence (PL) spectroscopy. X-ray diffraction analysis indicates that the pure cubic phase YAG was formed and strongly depends on the cerium content and the annealing temperature. It was found that the grain size ranges from 30 to 58 nm depending on the calcination temperature. The YAG:Ce nanophosphors showed intense, green-yellow emission, corresponding to Ce^{3+} $5d_1 \rightarrow {}^2F_{5/2}, {}^2F_{7/2}$ transitions and its photoluminescence excitation spectrum contains the two Ce^{3+} $4f^1 \rightarrow 5d_1, 5d_2$ bands. The crystal filed splitting energy levels positions $5d_1$ and $5d_2$ and the emission transitions blue shift with annealing temperatures have been discussed. It was found that the Ce^{3+} $4f^1$ ground state position relative to valence band maximum of YAG host nanomaterial decreases with increasing the temperature.

1. Introduction

Yttrium aluminum garnet $Y_3Al_5O_{12}$ (YAG) exists in the cubic garnet structure and has received great attentions in various fields of advanced applications because of its excellent chemical stability, good optical properties, and high temperature creep resistance [1, 2]. The YAG structure can be easily doped with several rare earth ions, allowing emissions of wavelengths from the near-infrared to ultra violet. Trivalent cerium doped YAG (YAG:Ce) is extensively utilized for numerous applications, such as cathode-ray tubes [3], field emission displays [4], scintillations, and electroluminescent displays [5]. The most important application of the YAG:Ce powder is converting the blue light emitting diodes (LEDs) radiation into a very broad band yellow emission, which can be used as one of the most common methods for producing white light with a gallium nitride-based blue LED [6, 7]. An important number of investigations on the elaboration of YAG:Ce powders have been reported in the literature. Generally, YAG powders have been produced via solid state reaction by mixing Y_2O_3 and Al_2O_3 powders. The disadvantage of this kind of reaction was the high reaction temperature (~1600°C), long heating time, milling process, and difficulty to obtain a homogeneous product and to control grain size [8]. Recently, many chemical methods have been successfully used to synthesize YAG nanopowders, such as precipitation [9], coprecipitation [10, 11], combustion [12], Pechini [13], solvothermal [14], polyacrylamide gel method [15], and sol-gel method [16, 17]. The sol-gel method has become very popular due to its versatility, better purity, low processing temperature, and the possibility of controlling the size and morphology of grains. Specifically, one of the most important features of doped sol-gel materials was their ability for providing uniform distribution of the dopant within the liquid host phase. To the best of our knowledge, the luminescence properties of YAG:Ce single crystal are well known for many years ago as phosphor and scintillator, but so far the material at the nanoscale remains poorly understood.

In the present paper, we report the preparation of nanosized Ce-doped YAG phosphor powders by a sol-gel process. The effect of annealing temperature on structural and photoluminescence properties is investigated. Furthermore, the main goal of this work is to study the blue shift origin of Ce^{3+} emission. We focus our attention in the relation between the 4f ↔ 5d interconfigurational excitation and emission transitions and $4f^1$ ground sate position of Ce^{3+} ion relative to the maximum of valence band of YAG host nanomaterial.

2. Experimental

2.1. Samples Preparation. The materials Y_2O_3 (99.99%), $Al(NO_3)_3$, $9H_2O$ (99.0%), Ce $(NO_3)_3$, $6H_2O$ (99.0%), nitric acid (HNO_3), citric acid (CH_3COOH), ethylene glycol ($HOCH_2CH_2OH$), and ammonia (NH_3) of analytical grade have been used as starting materials. The procedure of synthesis cerium-doped yttrium aluminum garnet with various concentrations 0.1, 0.5, 1.0, and 2.0 mol% Ce^{3+} and annealing temperature was described below. In the first step, a stoichiometric Y_2O_3 was dissolved in 100 mL of deionized water, previously mixed with 3 mL of nitric acid (HNO_3). After that, mixed solution was stirred at 80°C for 1 h to yield a clear and homogeneous solution. In the second step, a stoichiometric aluminum nitrate was dissolved to the resultant solution at a molar ratio, Y : Al, of 3 : 5. The corresponding stoichiometric of cerium nitrate was added to the solution. Then citric acid (CA) was added to the solution with molar ratio CA : M^{3+} = 1 (M^{3+} : Y^{3+} + Al^{3+} + Ce^{3+}), and subsequently ethylene glycol (EG) was added at a molar ratio EG : CA of 2 : 1. The solution was continuously stirred for several hours. The pH value of the solutions was adjusted to the desired value (pH = 1) by ammonia solution (NH_3). The resulting solution was dried at 120°C until foam was formed. For all Ce^{3+} concentrations, the foam was annealed in air at 1000°C for 4 hours under programmable oven. The same steps were followed for preparing calcined samples with a fixed concentration of cerium at 0.5 mol% Ce^{3+}, which corresponds to the maximum of luminescence intensity. Then the powders were annealed at various temperatures: 800, 850, 900, 950, 1000, 1050, and 1150°C for 4 hours.

2.2. Characterization of Samples. The phase identification and the related properties of the product powders were investigated by X-ray diffraction (XRD) technique, a PANanlytical X'Pert (Philips) PRO using CuK_α radiation (λ = 1.54059 Å) operated at 45 kV and 40 mA. Symmetric (θ-θ) scans were performed from 10° to 90° for 2θ values with a step width of 0.02°. All the data were processed by X'Pert HighScore plus Software with commercial databases (FWHM deduction and peaks identification). Thermal gravimetric analysis (TGA) of the precursor gel was recorded on a SETARAM Labsys TG-DTA 12 instrumentation from room temperature to 1000°C in 1.8 L/h of Ar with a heating rate of 10°C/min. Differential scanning calorimetry (DSC) of YAG precursors was performed using a SETARAM Setsys Instrumentation. The precursors were weighed to 28.6 mg and placed into an alumina crucible compared to a second empty one used as a reference. DSC trace was recorded between 25°C and 1000°C with a ramp rate of 10°C/min under 40 mL/min N_2 gas. The infrared spectra were recorded in the range of 400–4000 cm^{-1} using a Nicolet-IR 380 Fourier transform infrared (FTIR) spectrometer. Room temperature steady photoluminescence (PL) spectra were carried out using Perkin-Elmer (LS-50B) luminescence spectrometer, utilizing Xenon lamp as excitation source. The spectra were corrected for wavelength-dependent detection efficiency using the correction curve delivered by the spectrometer supplier. The emission spectra were plotted as relative emitted energy per constant energy interval as recommended for broad emission bands [18].

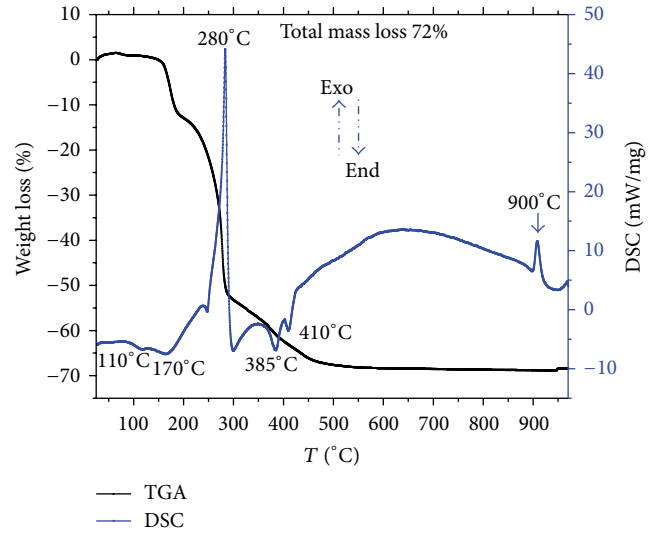

Figure 1: TG-DSC curves of the YAG precursor synthesized by sol-gel method.

3. Results and Discussion

3.1. Structural Analysis

3.1.1. Thermal Analysis. Figure 1 shows the TG-DSC curves of the as-dried gel with a heating rate of 10°C/min from 25 to 1000°C. It is found that the sample weight decreases with increasing temperature continuously from room temperature to 1000°C and the total mass loss is about 72 wt%. The first one weight loss of about 13.8% is due to desorption of water molecules from the surface. The second major weight loss observed around 280°C represents 48.32%, which is attributed to the disappearance of residual organic materials, while a minor weight loss was observed at 600°C, and beyond this temperature, a stable powder is obtained. In DSC curve, many endothermic and exothermic peaks are observed. Indeed, the two endothermic peaks observed at around 110 and 170°C correspond to water evaporation [19–21] and at 385°C to CO_2 and NO_3 decomposition [22, 23]. The peak at 410°C is assigned to the free carbon oxidation [24]. The exothermic peak at 280°C is due to the organic compounds combustion [25] and the other at 900°C represents the YAG crystallization temperature and is lower than that found very recently by Ji et al. [26] at 948°C, prepared by coprecipitation

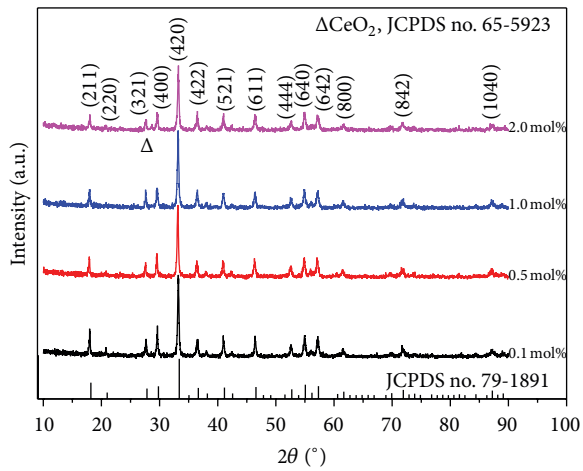

Figure 2: XRD patterns of Ce-doped YAG powders annealed at 1000°C for 4 h for different cerium concentration.

method. We thought that the difference in the method of preparation is the reason. Indeed, we think that using sol-gel method the crystallite grows more quickly than by coprecipitation method.

Figure 2 shows the X-ray diffraction patterns recorded at room temperature of Ce-doped YAG powders with different concentrations of cerium and calcined at 1000°C for 4 h. All the detectable diffraction peaks in Figure 2 can be well indexed in the cubic structure $Y_3Al_5O_{12}$ with space group Ia3d according to the JCPDS card number: 79-1891. It is noted that no intermediate phases of $YAlO_3$ (YAP) and $Y_4Al_2O_9$ (YAM) were detected. Except for sample prepared with 2.0 mol% Ce^{3+}, we observe the onset of another foreign peak (2θ~28.61°) at the YAG phase, which was attributed to the phase of CeO_2 (JPCDS card number 65-5923). However, it is observed that the intensities of diffraction peaks decrease when the concentration of cerium increases.

Figure 3(a) shows the XRD patterns of YAG:0.5% Ce^{3+}, calcined at different temperatures 800, 850, 900, 950, 1000, 1050, and 1150°C for 4 hours. It has been observed that the powders calcined at 800°C and 850°C show characteristics of the amorphous phase. When calcination temperatures increase up to 900°C, strong XRD patterns of pure YAG appear, well matched with JCPDS card number 79-1891, and result in good agreement with the above TG-DSC analysis. In addition, when the annealing temperature increases, the diffraction peaks become more intense and narrow, indicating an improved crystallinity.

The crystallographic unit cell parameters such as average crystallite size and the crystal lattice strain generated by increasing Ce^{3+} concentration and annealing temperature were determined. The average grain size was calculated by Scherrer [27] and Williamson-Hall relationships [28], respectively, as follows:

$$D_{\mathrm{Sch}} = \frac{0.9 \times \lambda}{\beta_{\mathrm{sample}} \cos\theta} \quad (1)$$

$$\frac{\beta \cos\theta}{\lambda} = \frac{1}{D_{\mathrm{will}}} + \frac{\varepsilon \sin\theta}{\lambda}. \quad (2)$$

Table 1: Structural parameters of cerium different concentration doped YAG samples.

	Cerium concentration			
	0.1 mol%	0.5 mol%	1 mol%	2 mol%
a (Å)	12.02	12.036	12.039	12.04
D_{scherrer} (nm)	33	32	29	28
$D_{\mathrm{williamson\text{-}Hall}}$ (nm)	68	45	42	28
Strain ε	0.00855	0.00682	0.00564	−0.00154

Table 2: Structural parameters of the 0.5 at% Ce^{3+}-doped YAG samples at different annealing temperatures.

	Annealing temperature				
	900°C	950°C	1000°C	1050°C	1150°C
a (Å)	12.044	12.043	12.038	12.031	12.020
D_{scherrer} (nm)	23	30	32	34	40
$D_{\mathrm{williamson\text{-}Hall}}$ (nm)	30	42	45	55	58
Strain ε	0.098	0.106	0.166	0.068	0.144

From Scherrer formula, the calculations were made from the intense diffraction peak corresponding to the plane (420) of YAG structure, where D is the crystallites size in nm, λ is the diffractometer wavelength in nm, $\beta_{\mathrm{sample}} = \sqrt{\beta_{\mathrm{exp}}^2 - \beta_{\mathrm{ins}}^2}$, β_{exp} is the full width at half maximum (FWHM) in the (420) reflection, β_{ins} is the correction factor for instrument broadening, and θ is the diffraction angle. The strain was calculated from the slope of the plot of $\beta\cos\theta/\lambda$ against $\sin\theta/\lambda$ and the effective grain size is calculated from the intercept to $\beta\cos\theta/\lambda$, respectively [29]. Moreover, the lattice parameter (a) and cell volume (V) were determined after refinement of structure using HighScore plus Software program. The estimated crystallites size, microstrain, and crystallographic unit as a function of cerium concentration and annealing temperature are illustrated in Tables 1 and 2, respectively. As seen in Table 1, the crystallite size value decreases when increasing cerium content. This later confirms the deterioration in the crystallinity of the powders. This effect can be explained if we consider that cerium atoms do not substitute yttrium atoms and occupy interstitial sites, resulting in a large number of dislocations or formation of compound growing along the YAG:Ce structure. At the same time, the strain can be positive (tensile) for samples doped with 0.1, 0.5, and 1.0 mol% or negative (compressive) for sample prepared with 2.0 mol%. Furthermore, the lattice parameter increases with increasing of cerium content value greater than theoretical value they should be (a = 12.017 Å for YAG, JCPDS number 79-1891). This difference can be explained by the disorder of the crystalline network that, due to the effective radius of Ce^{3+} (1.034), is bigger than that of Y^{3+} (0.900) [30].

The reduction of the lattice parameter and the increase in the grain size from 30 to 58 nm with the increasing of the annealing temperature, as shown in Figure 3(b), signify the closeness of lattice plane which can lead to an increase in the density and the decrease of dislocation density. The same observation has been made by Boukerika and Guerbous

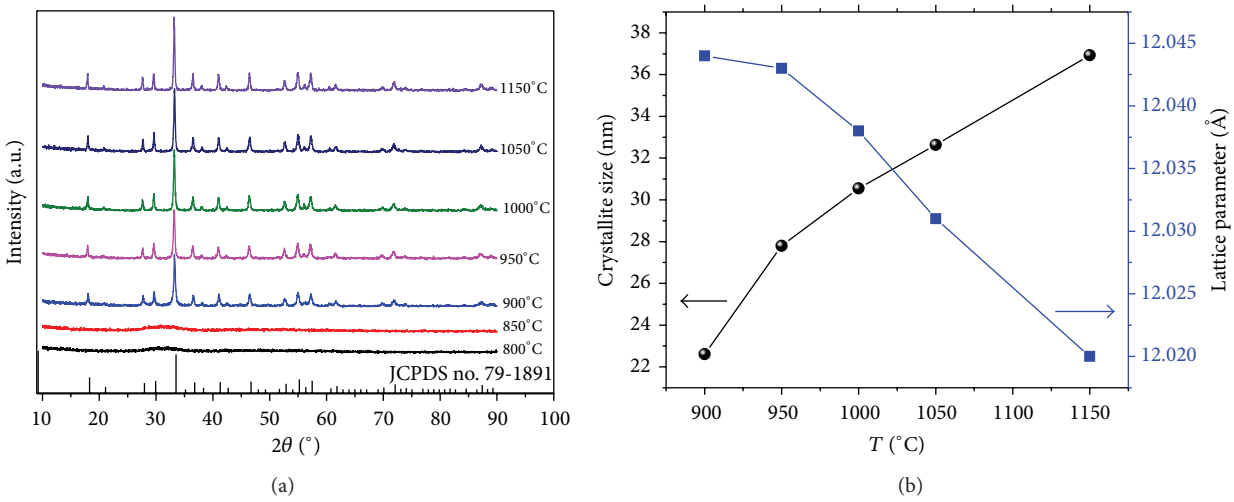

FIGURE 3: (a) XRD patterns of YAG:0.5 at% Ce^{3+} powders annealed at different annealing temperature and (b) YAG:0.5 at% Ce^{3+} grain size and lattice parameter evolution in function of annealing temperature.

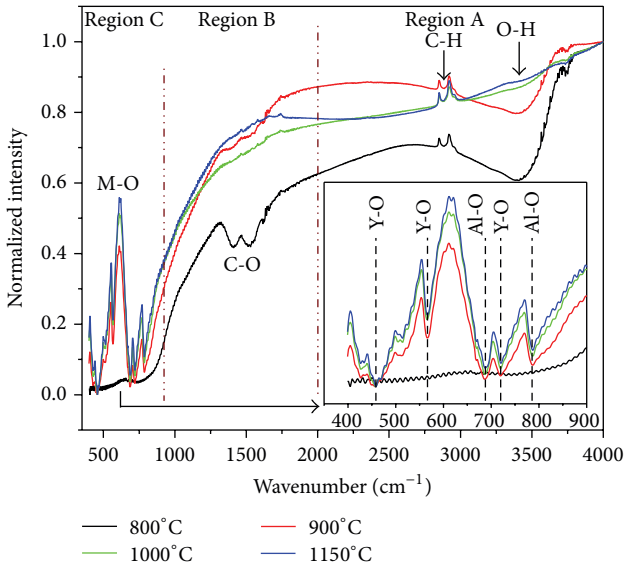

FIGURE 4: FTIR spectra of YAG:0.5 at% Ce^{3+} samples annealed at 800, 900, 1000, and 1150°C.

[29] in $Y_2O_3:Eu^{3+}$ system. The grain size estimated by W-H method is always greater than those estimated by Scheerer, indicating that the strain has a contribution in peak broadening, but its evolution in function of annealing temperature is not clear.

3.1.2. FTIR Analysis. The synthesis of YAG:0.5 at% Ce^{3+} phosphor of high quality involves determining the optimal annealing temperature necessary to obtain a crystallized powder devoid of organic compounds. The FTIR analysis was used to study the organic residua evolution with annealing temperature. FTIR transmission spectra of the powder annealed at 800, 900, 1000, and 1150°C are given in Figure 4. It is found that the characteristic bands of organic residues are observed and may be divided into three regions. In Region A, above 2000 cm^{-1}, it is observed that the band around 2900 cm^{-1} corresponds to the stretching vibration of the C-H [20], and a broad absorption band at approximately 3450 cm^{-1}, which is a characteristic of stretching vibration of groups O-H [6, 31], caused by the adsorption of molecular water from KBr pellet technique forms preparation sample. In Region B, the bands between 1200 and 1500 cm^{-1} and the main band localized at 1510 and 1387 cm^{-1} are assigned to C-O asymmetric stretching vibration. As the annealed temperature increases, the double absorption peaks corresponding to C-O disappear, implying the decomposition of CO_3^{2-} [32]. The absorption bands intensities of O-H and C-O groups decrease with the increase of annealing temperature.

In Region C, in the range from 400 to 900 cm^{-1}, the absorption bands localized at 457, 567, 687, 720, and 786 cm^{-1} are ascribed to the metal-oxygen vibration characteristics of M-O (M = Y, Al) stretches, confirming the formation of a YAG phase [33, 34]. Moreover, it is clearly observed in Figure 8 (inset) that the sample annealed at 800°C does not present the characteristic peaks of metal-oxygen (Y-O or Al-O); this can be related to the formation of an amorphous phase. These results were in good agreement with XRD measurement (see Figure 3(a)). Also, it was observed that the M-O absorption band increased with the increases of annealing temperature, which indicates an improvement in crystallinity of the powders.

3.2. Steady Photoluminescence Spectroscopy and 4f-5d Transitions Analysis in YAG Host Nanomaterial. In order to study the grain size effect of 4f-5d interconfigurational transitions, room temperature emission and excitation spectra are recorded. Figure 5 displays the excitation and the emission spectra of YAG:0.5 at% Ce^{3+} samples annealed at different temperatures. For 800 and 850°C annealing temperatures, which reveal an amorphous phase, under UV (340 nm) and

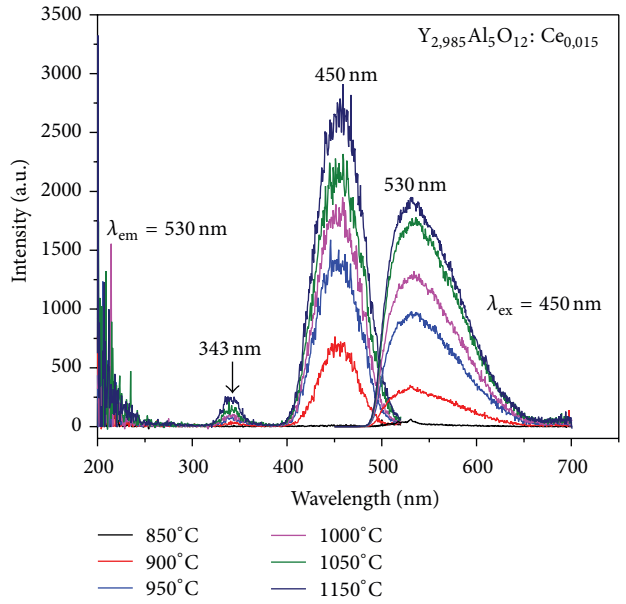

FIGURE 5: Room temperature emission and excitation spectra of YAG:0.5 at% Ce^{3+} nanophosphor powders, under excitation 450 nm wavelength and fixed emission wavelength at 530 nm for different annealing temperature.

blue (450 nm) excitations (corresponding to 5d excitation levels), no Ce^{3+} emission is observed. The crystallization of the phase YAG triggers when the temperature reached 900°C and from this calcination temperature a broad emission band corresponding to the parity-allowed electric dipole transition 5d → 4f was observed and begins to be refined reflecting the densification powder structure. The emission spectra are constituted by broad and asymmetric band emission centered at about 530 nm attributed to transition from the lowest crystal field component of $5d^1$ to the two levels of the ground state $^2F_{5/2}$ and $^2F_{7/2}$, separated by around 2000 cm^{-1} due to spin–orbit coupling. It may be noted that the fluorescence emission of our powders increases progressively with the heat treatment temperature. In fact, this effect can be explained by the improvement of the degree of crystallinity and decrease of surface defects as a function of heat treatment temperature. Similar results have been previously reported by Fadlalla and Tang [5]. Indeed, annealing sample may improve the substitution of Ce^{3+} ions into Y lattice in the YAG matrix with good incorporation of Ce^{3+} ions that can contribute to the enhancement of emission intensity [6, 35]. In addition, we note that in our results Ce^{3+}-doped YAG presented a blue shift as the annealing temperature increases, instead of red shift as observed by other authors [1, 36].

The excitation spectra, measured for 530 nm emission wavelength (corresponding to Ce^{3+} emission), are shown in the same figure. Indeed, for all annealing temperatures above 900°C, the excitation spectra present two broad absorption bands: the first one is a very intense and broad band localized at 450 nm and the second is a low intensity broad band centered at 340 nm. These bands can be attributed to the allowed electric-dipole transitions from $4f^1$ ground state to the first and the second 5d excited states of the same ion. It is well known that the 5d electron experiences much stronger interactions with the crystal field than does the 4f electron because of the large radial extension of the 5d orbitals. Furthermore, the 4f-5d excitation and emission bands are widely vibronic in character; consequently, the decomposition of emission and excitation spectra into a sum of Gaussian curves is justified [37]. In addition, we note that energy 5d levels positions remain as the grain size increases, despite the blue shift observed in emission spectra.

Figure 6 illustrates the emission spectra of Ce^{3+}-doped YAG nanophosphor, fitted into two Gaussian curves, which represent the 5d → $^2F_{5/2}$, $^2F_{7/2}$ interconfigurational transitions at room temperature. We note from Figure 6 that the high energy transition (5d → $^2F_{5/2}$) becomes more intense compared to the lower energy (5d → $^2F_{7/2}$) as soon as the grain size increases, indicating that the self-absorption in Ce^{3+}-doped YAG increases. The spectroscopic parameters such as transitions energy values, difference between energy transitions, zero phonon line (ZPL) position, and Stokes shift are presented in Table 3. Several observations can be made from the values of spectroscopic parameters, summarized in Figure 7: as the grain size increases, the Gaussian curves positions have blue shifted, the difference in energy (ΔE) between the two energy transitions 5d → $^2F_{5/2}$, $^2F_{7/2}$ deceases, the ZPL position decreases, and the Stokes shift (ΔE_S) increases.

The decreasing in ΔE with grain size is related by several authors to the decreasing in crystal field related to the decreasing in lattice parameter, which is in agreement with our results. The small value of the Stokes shift corresponded to the small grain size and has been already explained by stiffness of the crystal surrounding nanophosphors and the equilibrium distance of Ce^{3+} with its ligands in nanophosphors was short [38]. Furthermore, it is known that increasing Stokes shift leads to an emission red shift. Indeed, according to Blasse and Bril [39], there are two cases in which the emission will be at lower wavenumbers (red shifted): if the lowest 5d level lies exceptionally low and if the Stokes shift of emission is exceptionally large. Also, several authors have observed that Ce^{3+} emission of the YAG:Ce^{3+} nanocrystals was blue shift as compared with the YAG bulk and is explained by the decrease of lattice constant that affects the crystal field around Ce^{3+} ions [40, 41], which are in opposition to our results. To explain this phenomenon, we have considered two models. The first one is Meltzer model [42] related to the refractive index of nanomaterial. The second one is the empirical model of Thiel and Cone [43], predicting the energy distance between rare earth trivalent ground state and the maximum of the valence band of host material. In our approach, we concentrate our attention on the evolution of this energy distance between rare earth ground state 4f and the valence as a function grain size.

Thiel and Cone [43] have proposed an empirical model that describes and predicts the variation in 4f electrons energies of the lanthanide ions in several inorganic compounds based only on the materials refraction index. According to Thiel model, we can estimate the position of the $4f^N$ ground

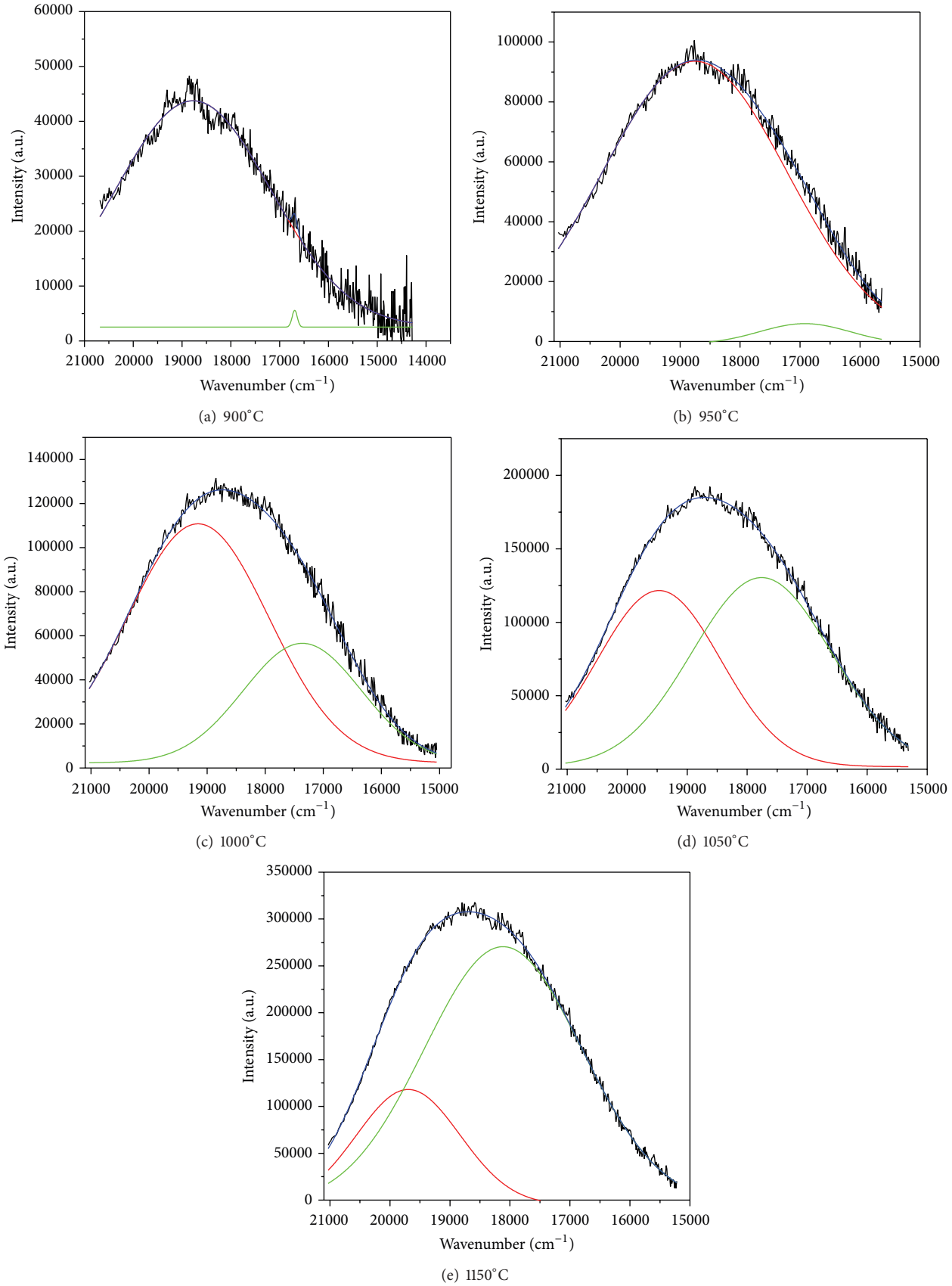

Figure 6: Decomposition into sum of two Gaussian curves of different annealing temperature emission spectra of YAG:0.5 at% Ce^{3+}.

Table 3: Spectroscopic parameters of YAG:0.5 at% Ce^{3+}.

Temperature (°C)	Transition energy (cm^{-1}) $5d \rightarrow {}^2F_{5/2}$	Transition energy (cm^{-1}) $5d \rightarrow {}^2F_{7/2}$	ΔE (cm^{-1})	Zero phonon line energy (ZPL) (cm^{-1})	Stokes shift ΔE_S (cm^{-1})
850	—	—	—	—	—
900	18754	16691	2081	21219	2012
950	18773	16920	1834	20684	2865
1000	19157	17360	1796	20625	2983
1050	19469	17759	1710	20508	3217
1150	19694	18115	1579	20499	3235

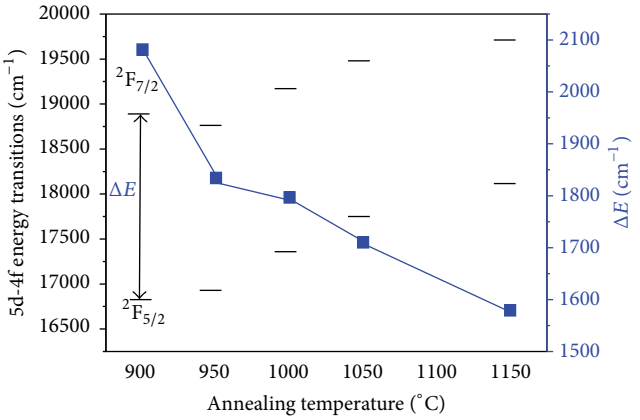

Figure 7: Variation $5d_1 \rightarrow {}^2F_{5/2}$, $^2F_{7/2}$ energy transitions and the distance in energy between $^2F_{5/2}$ and $^2F_{7/2}$ spin-orbit energy levels ΔE in function of annealing temperature.

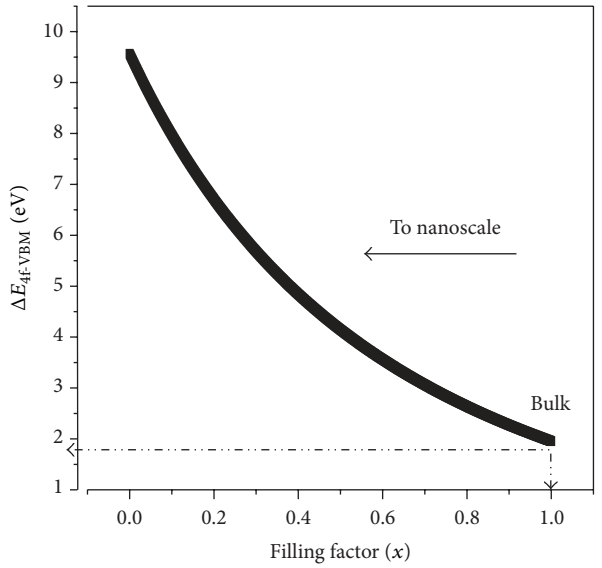

Figure 8: Variation of $\Delta E_{4f\text{-}VBM}$ against the filling factor x.

state relative to the valence band maximum called $\Delta E_{4f\text{-}VBM}$ using the following expression:

$$\Delta E_{4f\text{-}VBM} \approx I_f - 37.0\,\text{eV} - \left(\frac{10.9\,\text{eV}}{n^2}\right) - 0.13\,\text{eV}\,(A - 67), \tag{3}$$

where I_f is the free ion ionization potential, n is the host materials refraction index in the visible region, and A is the atomic number of the trivalent lanthanide.

It is known that the nanoparticles occupy only a small fraction of the total volume; then, it is necessary to introduce an effective index of refraction for the medium, n_{eff}, which consists of the nanoparticles surrounded by the media with refractive index n_{med}. One may evaluate an effective refraction index [44]. Consider

$$n_{\text{eff}}(x) = x n_{\text{NP}} + (1 - x)\, n_{\text{med}}, \tag{4}$$

where x is the "filling factor" showing which fraction of space is occupied by the nanoparticles. For nanoparticles, n in (3) is consequently replaced by $n_{\text{eff}}(x)$ (4). The use of n_{eff} is valid when the average size of the particles is much smaller than the wavelength of light, which is true in this study. For the YAG bulk material, n (YAG) = 1.82 [43] and the medium in which the YAG:Ce^{3+} nanophosphor is putted is the air; $n_{\text{med}} = n_{\text{air}} = 1$. Consequently, for YAG nanophosphor, we can write

$$n_{\text{eff}}(x) = 0.82x + 1. \tag{5}$$

Replacing n_{eff} in (3), we obtain

$$\Delta E_{4f\text{-}VBM} \approx I_f - 37.0\,\text{eV} - \left(\frac{10.9\,\text{eV}}{(n_{\text{eff}})^2}\right) - 0.13\,\text{eV}\,(A - 67) \tag{6}$$

$$\Delta E_{4f\text{-}VBM} \approx I_f - 37.0\,\text{eV} - \left(\frac{10.9\,\text{eV}}{(0.82x + 1)^2}\right) - 0.13\,\text{eV}\,(A - 67). \tag{7}$$

For Ce^{3+}, $I_f = 36.757$ eV [42], $A = 55$, and (7) becomes

$$\Delta E_{4f\text{-}VBM}(x) \approx 1.317 - \left(\frac{10.9\,\text{eV}}{(0.82x + 1)^2}\right). \tag{8}$$

Figure 8 displays the evolution of $\Delta E_{4f\text{-}VBM}$ against the filling factor x. For $x = 1$ corresponding to the single crystal [1], $\Delta E_{4f\text{-}VBM} = 1.95$ eV. With the standard deviation around 0.7 eV [43], we obtain a value of 2.65 eV. The photoconductivity measurements [45] on YAG:Ce^{3+} indicate that Ce^{3+} $4f^1$ ground state is situated at 2.7 eV above the valence band maximum, which is not far from our prediction value.

For each grain size "D" corresponding to a filling factor value x, the difference in energy between the two

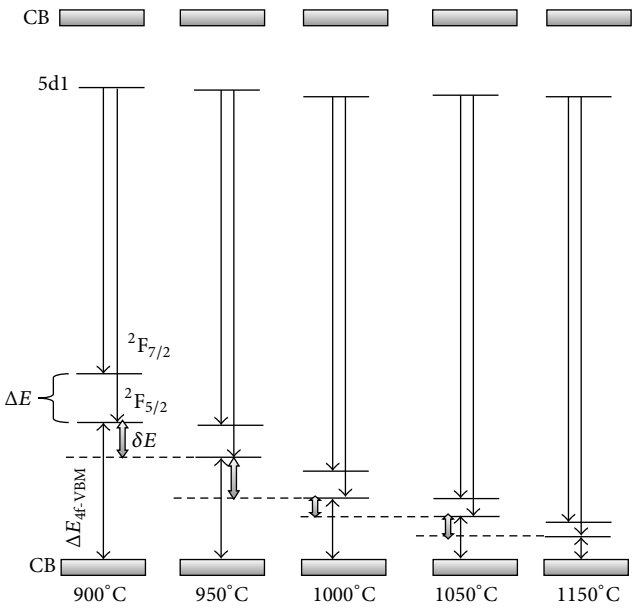

FIGURE 9: Schematic Ce^{3+} energy level diagram relative to YAG host bands in different annealing temperature; the different energy quantities are shown.

corresponding $\Delta E_{4f\text{-VBM}}(x)$ is called δE. This later is the same as the difference between 5d $\rightarrow$ 4f energy transitions corresponding to two grain sizes. Figure 9 depicts a schematic Ce^{3+} energy level diagram in different temperatures (grain size). From this figure, we write energy balance as follows:

$$\left[E_{5d\rightarrow {}^2F_{5/2}}(x_1) - E_{5d\rightarrow {}^2F_{5/2}}(x_2)\right] = \left[\Delta E_{4f\text{-VBM}}(x_1) - \Delta E_{4f\text{-VBM}}(x_2)\right] = \delta E. \quad (9)$$

Then,

$$\delta E = 10.9\,\text{eV}\left(\frac{1}{(0.82x_1+1)^2} - \frac{1}{(0.82x_2+1)^2}\right). \quad (10)$$

Experimentally, we determinate δE from emission spectra and knowing only one value of x corresponding to a given grain size of Ce^{3+}-doped YAG, we can determine all the filling factors. Consequently, from (8), the blue shift increases with the grain size which explains well our experiment results.

The remaining 5d energy levels positions in the same values, despite the emission blue shift, can be related to the very recent new effect observed by Feofilov et al. [46]. Indeed, according to these authors, in Ce^{3+}-doped YAG crystalline and nanocrystalline, Ce^{3+} fluorescence is observed even upon excitation well below the $4f^1 \rightarrow 4f^05d^1$ zero phonon line (ZPL). For $T_1 = 900^\circ C$ and $T_2 = 1150^\circ C$ annealing temperature, which represents the lower and the higher points in our studies, we find that $\delta E = 940\,cm^{-1}$. This value is less than $1650\,cm^{-1}$, below the zero phonon line (ZPL) of the $4f^1$ ($^2F_{5/2}$) $\rightarrow$ $4f^05d^1$ transition located at 489 nm ($20449\,cm^{-1}$) observed by Feofilov et al. [46] and in agreement with our ZPL value (Table 3). For this reason, we thought that δE presents an additional energy which can be derived from YAG phonons and help well below ZPL energy to excite 5d levels.

4. Conclusion

Nanoscaled pure cubic phase cerium doped yttrium aluminum garnet (YAG:Ce) phosphor was successfully synthesized by sol-gel method. The phase formation, the organic compounds evolution, and the steady photoluminescence property variation were fully investigated and found to be strongly dependent on the cerium content and the heat treatment temperature. The crystallite size has been found to increase from 30 to 58 nm when increasing annealing temperature. An intense green-yellow luminescence, corresponding to $5d_1 \rightarrow {}^2F_{5/2}$, $^2F_{7/2}$ interconfigurational spin-allowed electric dipole transitions of Ce^{3+} in YAG nanophosphor powders, is observed. The two $5d_1$ and $5d_2$ energy levels resulting from crystal field splitting of 5d state are localized and remain still in the same position independently of calcination temperature. The phonons of YAG material can give supplementary energy to that of well below $4f^1 \rightarrow 4f^05d^1$ zero phonon line to excite 5d levels. The increasing in Stokes shift value with grain size does not prevent a blue shift of luminescence. The distance in energy between the $4f^1$ ground state position of Ce^{3+} and valence band maximum of YAG host nanomaterial is found to be weaker as the grain size increases, which explained the emission blue shift.

Conflict of Interests

The authors declare that there is no conflict of interests regarding the publication of this paper.

References

[1] A. Speghini, F. Piccinelli, and M. Bettinelli, "Synthesis, characterization and luminescence spectroscopy of oxide nanopowders activated with trivalent lanthanide ions: the garnet family," *Optical Materials*, vol. 33, no. 3, pp. 247–257, 2011.

[2] Y. Lv, W. Zhang, H. Liu et al., "Synthesis of nano-sized and highly sinterable Nd:YAG powders by the urea homogeneous precipitation method," *Powder Technology*, vol. 217, pp. 140–147, 2012.

[3] Y. C. Wu, S. Parola, O. Marty, M. Villanueva-Ibanez, and J. Mugnier, "Structural characterizations and waveguiding properties of YAG thin films obtained by different sol-gel processes," *Optical Materials*, vol. 27, no. 9, pp. 1471–1479, 2005.

[4] H. M. H. Fadlalla, C. C. Tang, S. Y. Wei, and X. X. Ding, "Preparation and properties of nanocrystalline powders in $(Y_{1-x}Ce_x)_3Al_5O_{12}$ system," *Journal of Luminescence*, vol. 128, no. 10, pp. 1655–1659, 2008.

[5] H. M. H. Fadlalla and C. Tang, "Sol-gel preparation and photoluminescence properties of Ce^{3+}-activated $Y_3Al_5O_{12}$ nanosized powders," *Journal of Crystal Growth*, vol. 311, no. 14, pp. 3737–3741, 2009.

[6] P. Rai, M.-K. Song, H.-M. Song et al., "Synthesis, growth mechanism and photoluminescence of monodispersed cubic

shape Ce doped YAG nanophosphor," *Ceramics International*, vol. 38, no. 1, pp. 235–242, 2012.

[7] Y. Li and R. M. Ameida, "Preparation and optical properties of sol-gel derived thick YAG:Ce^{3+} phosphor film," *Optical Materials*, vol. 34, pp. 1148–1154, 2012.

[8] D. Lozano-Mandujano, J. Zárate-Medina, R. Morales-Estrella, and J. Muñoz-Saldaña, "Synthesis and mechanical characterization by nanoindentation of polycrystalline YAG with Eu and Nd additions," *Ceramics International*, vol. 39, no. 3, pp. 3141–3149, 2013.

[9] H. M. H. Fadlalla and C. C. Tang, "YAG:Ce^{3+} nano-sized particles prepared by precipitation technique," *Materials Chemistry and Physics*, vol. 114, no. 1, pp. 99–102, 2009.

[10] M. Zeng, Y. Ma, Y. Wang, and C. Pei, "The effect of precipitant on co-precipitation synthesis of yttrium aluminum garnet powders," *Ceramics International*, vol. 38, no. 8, pp. 6951–6956, 2012.

[11] W. Zhang, J. Cen, Z. Hu, H. Wu, X. Sheng, and L. Luo, "Co-precipitation synthesis and luminescent properties of indium-substituted YAG: Ce^{3+}," *Advanced Powder Technology*, vol. 24, no. 1, pp. 21–25, 2013.

[12] L. Yang, T. Lu, H. Xu, and N. Wei, "Synthesis of YAG powder by the modified sol-gel combustion method," *Journal of Alloys and Compounds*, vol. 484, no. 1-2, pp. 449–451, 2009.

[13] S. A. Hassanzadeh-Tabrizi, "Synthesis and luminescence properties of YAG:Ce nanopowder prepared by the Pechini method," *Advanced Powder Technology*, vol. 23, no. 3, pp. 324–327, 2012.

[14] A. Bhaskar, H.-Y. Chang, T.-H. Chang, and S.-Y. Cheng, "Microwave annealing of YAG: Ce nanophosphors," *Materials Letters*, vol. 78, pp. 124–126, 2012.

[15] C.-J. Liu, R.-M. Yu, Z.-W. Xu, J. Cai, X.-H. Yan, and X.-T. Luo, "Crystallization, morphology and luminescent properties of YAG:Ce^{3+} phosphor powder prepared by polyacrylamide gel method," *Transactions of Nonferrous Metals Society of China*, vol. 17, no. 5, pp. 1093–1099, 2007.

[16] T. Ogi, A. B. D. Nandiyanto, W.-N. Wang, F. Iskandar, and K. Okuyama, "Direct synthesis of spherical YAG:Ce phosphor from precursor solution containing polymer and urea," *Chemical Engineering Journal*, vol. 210, pp. 461–466, 2012.

[17] E. de la Rosa, L. A. Díaz-Torres, P. Salas et al., "Low temperature synthesis and structural characterization of nanocrystalline YAG prepared by a modified sol-gel method," *Optical Materials*, vol. 27, no. 12, pp. 1793–1799, 2005.

[18] G. Blasse and B. C. Grabmaier, *Luminescent Materials*, Springer, Berlin, Germany, 1994.

[19] H. Gong, D.-Y. Tang, H. Huang et al., "Crystallization kinetics and characterization of nanosized Nd:YAG by a modified sol-gel combustion process," *Journal of Crystal Growth*, vol. 362, no. 1, pp. 52–57, 2013.

[20] S. Yang, W. Que, J. Chen, and W. G. Liu, "Nd:YAG nano-crystalline powders derived by combining co-precipitation method with citric acid treatment," *Ceramics International*, vol. 38, no. 4, pp. 3185–3189, 2012.

[21] S. A. Hassanzadeh-Tabrizi, E. Taheri-Nassaj, and H. Sarpoolaky, "Synthesis of an alumina-YAG nanopowder via sol-gel method," *Journal of Alloys and Compounds*, vol. 456, no. 1-2, pp. 282–285, 2008.

[22] P. Ramanujam, B. Vaidhyanathan, J. Binner, A. Anshuman, and C. Spacie, "A comparative study of the synthesis of nanocrystalline Yttrium Aluminium Garnet using sol-gel and co-precipitation methods," *Ceramics International*, vol. 40, no. 3, pp. 4179–4186, 2014.

[23] Q. Lu, W. Dong, H. Wang, and X. Wang, "A novel way to synthesize yttrium aluminum garnet from metal-inorganic precursors," *Journal of the American Ceramic Society*, vol. 85, no. 2, pp. 490–492, 2002.

[24] J. Li, Y. Pan, F. Qiu, Y. Wu, and J. Guo, "Nanostructured Nd:YAG powders via gel combustion: the influence of citrate-to-nitrate ratio," *Ceramics International*, vol. 34, no. 1, pp. 141–149, 2008.

[25] R. C. Pullar and A. K. Bhattacharya, "Polycrystalline yttrium aluminium garnet (YAG) fibres produced from the steaming of an aqueous sol-gel precursor," *Materials Letters*, vol. 39, no. 3, pp. 173–178, 1999.

[26] X. Ji, B. Kang, J. Deng, H. Huang, and X. Wang, "Thermal decomposition and evolved gas analysis of neodymium-doped yttrium aluminum garnet precursor prepared by co-precipitation," *Thermochimica Acta*, vol. 552, pp. 23–27, 2013.

[27] S. A. Hassanzadeh-Tabrizi, "Low temperature synthesis and luminescence properties of YAG: Eu nanopowders prepared by modified sol-gel method," *Transactions of Nonferrous Metals Society of China*, vol. 21, no. 11, pp. 2443–2447, 2011.

[28] G. K. Williamson and W. H. Hall, "X-ray line broadening from filed aluminium and wolfram," *Acta Metallurgica*, vol. 1, no. 1, pp. 22–31, 1953.

[29] A. Boukerika and L. Guerbous, "Annealing effects on structural and luminescence properties of red Eu^{3+}-doped Y_2O_3 nanophosphors prepared by sol-gel method," *Journal of Luminescence*, vol. 145, pp. 148–153, 2014.

[30] R. D. Shannon, "Revised effective ionic radii and systematic studies of interatomic distances in halides and chalcogenides," *Acta Crystallographica Section A*, vol. 32, no. 5, pp. 751–767, 1976.

[31] D. Boyer, G. Bertrand-Chadeyron, and R. Mahiou, "Structural and optical characterizations of YAG:Eu^{3+} elaborated by the sol-gel process," *Optical Materials*, vol. 26, no. 2, pp. 101–105, 2004.

[32] Z.-H. Chen, Y. Yang, Z.-G. Hu, J.-T. Li, and S.-L. He, "Synthesis of highly sinterable YAG nanopowders by a modified co-precipitation method," *Journal of Alloys and Compounds*, vol. 433, pp. 328–331, 2007.

[33] Z. Sun, D. Yuan, H. Li et al., "Synthesis of yttrium aluminum garnet (YAG) by a new sol-gel method," *Journal of Alloys and Compounds*, vol. 379, no. 1-2, p. -L3, 2004.

[34] X. Li and W. Wang, "Preparation of uniformly dispersed YAG ultrafine powders by co-precipitation method with SDS treatment," *Powder Technology*, vol. 196, no. 1, pp. 26–29, 2009.

[35] A. A. Bol and A. Meijerink, "Luminescence quantum efficiency of nanocrystalline ZnS:Mn^{2+}: 1. Surface passivation and Mn^{2+} concentration," *The Journal of Physical Chemistry B*, vol. 105, no. 42, pp. 10197–10202, 2001.

[36] P. A. Tanner, L. Fu, L. Ning, B.-M. Cheng, and M. G. Brik, "Soft synthesis and vacuum ultraviolet spectra of YAG:Ce^{3+} nanocrystals: reassignment of Ce^{3+} energy levels," *Journal of Physics: Condensed Matter*, vol. 19, no. 21, Article ID 216213, 2007.

[37] L. Guerbous and O. Krachni, "The 4f-5d luminescence transitions in cerium-doped LuF3," *Journal of Modern Optics*, vol. 53, no. 14, pp. 2043–2053, 2006.

[38] L. T. Su, A. I. Y. Tok, F. Y. C. Boey, X. H. Zhang, J. L. Woodhead, and C. J. Summers, "Photoluminescence phenomena of Ce^{3+}-doped $Y_3Al_5O_{12}$ nanophosphors," *Journal of Applied Physics*, vol. 102, no. 8, Article ID 083541, 2007.

[39] G. Blasse and A. Bril, "Investigation of some Ce^{3+}-activated phosphors," *The Journal of Chemical Physics*, vol. 47, no. 12, pp. 5139–5145, 1967.

[40] G. Xia, S. Zhou, J. Zhang, and J. Xu, "Structural and optical properties of YAG:Ce^{3+} phosphors by sol-gel combustion method," *Journal of Crystal Growth*, vol. 279, no. 3-4, pp. 357–362, 2005.

[41] H.-J. Byun, W.-S. Song, Y.-S. Kim, and H. Yang, "Solvothermally grown Ce^{3+}-doped $Y_3Al_5O_{12}$ colloidal nanocrystals: spectral variations and white LED characteristics," *Journal of Physics D: Applied Physics*, vol. 43, no. 19, Article ID 195401, pp. 1–6, 1954.

[42] R. S. Meltzer, W. M. Yen, H. Zheng et al., "Effect of the matrix on the radiative lifetimes of rare earth doped nanoparticles embedded in matrices," *Journal of Luminescence*, vol. 94-95, pp. 217–220, 2001.

[43] C. W. Thiel and R. L. Cone, "Investigating material trends and lattice relaxation effects for understanding electron transfer phenomena in rare-earth-doped optical materials," *Journal of Luminescence*, vol. 131, no. 3, pp. 386–395, 2011.

[44] R. S. Meltzer, S. P. Feofilov, B. Tissue, and H. B. Yuan, "Dependence of fluorescence lifetimes of Y2O3:Eu^{3+} nanoparticles on the surrounding medium," *Physical Review B—Condensed Matter and Materials Physics*, vol. 60, no. 20, pp. R14012–R14015, 1999.

[45] C. W. Thiel, *Energies of rare-earth ion states relative to host bands in optical materials from electron photoemission spectroscopy [Ph.D. thesis]*, Montana State University USA, Bozeman, Mont, USA, 2003.

[46] S. P. Feofilov, A. B. Kulinkin, T. Gacoin et al., "Mechanisms for Ce^{3+} excitation at energies below the zero-phonon line in YAG crystals and nanocrystals," *Journal of Luminescence*, vol. 132, no. 11, pp. 3082–3088, 2012.